MEASUREMENT OF NATURAL FREQUENCY AND DAMPING OF A SLENDER MODEL IN MACH 5 FLOW

Benjamin Diaz Villa[1*], Marc A. Eitner[1], Jayant Sirohi[1], Noel T. Clemens[1]

[1] The University of Texas at Austin,
2617 Wichita St North Office Building A,
Austin, TX, 78712, USA
[*]benjamin.diazvilla@austin.utexas.edu

Abstract: Hypersonic vehicles that have a high slenderness ratio are prone to aerothermoelastic deformations that can affect maneuverability. The goal of this study is to assess the effectiveness of different types of structural excitation as well as damping extraction algorithms to identify the natural frequency and damping of a representative cone-cylinder model in Mach 5 flow. The conical and cylindrical sections were rigid, but were connected by a flexure element that restricted the cone's dynamics to a pitching motion only. This single degree of freedom system was excited in Mach 5 flow using two different structural excitation methods: exposing the model to free-stream turbulence, and harmonically forcing the structure with an embedded vibrating motor. These excitation techniques were used to infer the aerodynamic stiffness and aerodynamic damping using several analysis techniques. Algorithms such as the Random Decrement technique and the Natural Excitation technique were used to generate a free-decay response from the free-stream turbulence forcing cases. The Moving-Block technique and the Continuous Wavelet Transform were used to calculate the wind-on damping ratio from all wind-on signals. Wind-off and wind-on comparisons of the structure's natural frequency and damping ratio were made. Wind-on natural frequencies were measured to be lower than wind-off cases, while wind-on damping ratios were measured to be higher than the wind-off cases. These results indicate that aerodynamic forces contribute negative stiffness and positive damping to the system for this particular structural setup. In summary, both structural excitation methods prove useful for aeroelastic studies in long-duration hypersonic wind tunnels.

1   INTRODUCTION

Hypersonic vehicle design is inherently multi-disciplinary, combining aerodynamics, propulsion, structural dynamics, and controls [1]. This highly integrated design is necessary given the extreme and harsh conditions in which the vehicle is immersed. Consequently, this extreme flight regime imposes design constraints that are difficult to solve. One such constraint is the use of light-weight, thermally-resistant materials that leads to low stiffness in structures under high aerothermal loads. In addition, hypersonic flows are characterized by high temperatures, thin shock layers, strong viscous interactions, and shock wave boundary layer interactions. This gives rise to a variety of aeroelastic behavior along different regions of the vehicle, such as panel flutter, fin/control surface "flag-waving" flutter, cylindrical shell flutter, scramjet inlet cowling buffeting, and static

divergence just to name a few [2,3]. Not only are these aeroelastic behaviors taken into account when designing the vehicle, but they must also be understood when designing the control system and algorithms for the vehicle's performance and maneuverability. In addition, hypersonic vehicles that have a high slenderness ratio are prone to aerothermoelastic deformations that can affect maneuverability and impede overall control [4,5]. Therefore, studying and understanding the fluid-structure interaction (FSI) in hypersonic environments is critical for future successful hypersonic flights.

In recent years, results from the BOLT flight campaign showed that the BOLT vehicle (with a slenderness ratio of 15:1) exhibited unanticipated flight dynamics that resulted in a reduced apogee and a reduced velocity on descent due to aeroelastic effects [6]. Consequently, these unaccounted aeroelastic behaviors affected the expected boundary layer transition measurements. Similarly, it has been observed that gyroscopes that are placed far away from the vehicle's center of mass suffer from aeroelastic effects by sending erroneous and altered pitch-rate and pitch-angle feedback signals, leading to a large performance degradation in controls [5]. Similar work was also done to study the effect of intermittent turbulent spots from a slender 7-degree half-angle cone on the FSI of the downstream control surface in high Mach number flow [7]. In another experimental study, downstream aerodynamic effects were also investigated from upstream shell fluttering deformations in Mach 4 flow [8]. However, both experimental studies used noncompliant models with noncompliant upstream fuselages, and the latter experimental study simply replicated the shell deformation by machining the deformed outer-mold line.

In the current study, a single degree-of-freedom (SDOF) cone-cylinder model was designed by constraining the conical section to have only a pitching vibrational motion. Constraining the vibrational DOF to only pitch rotation was chosen because it has been observed from cited literature that only the first bending mode has a significant influence on the body stability [9,28].

The idea of reducing the vibrational DOF in order to analyze high-speed aeroelasticity is not new, especially within analytical and numerical studies [9,10]. However, this has been seldom done experimentally, especially when taking a systematic approach to limiting the DOF of the vehicle's internal structure within high-speed flows. In the end, the purpose for this project is to analyze the hypersonic FSI nature of low vibrational DOF structure models before analyzing continuously elastic wind tunnel models. In a similar fashion, this work establishes a baseline for which future multiphysics simulations of hypersonic ground testing can be validated before moving onto more complicated systems.

It has been observed that measuring aerodynamic damping remains crucial for aeroelastic analysis in hypersonic flows [11]. Whereas structural displacement leads to aerodynamic stiffness terms, the phase lag of fluid advection to the relative input motion leads to aerodynamic damping terms in the FSI governing equations [12]. One of the forces which are usually not measured in supersonic and hypersonic wind tunnels are the damping forces because they are not easy to isolate [13]. Determination of subcritical damping during flutter tests both in wind tunnels and in flight is a subject that still receives widespread attention. The need for subcritical damping data has long been recognized, but obtaining these data is not an easy task [14]. Subcritical damping and aerodynamic damping measurements have been done on low-speed wind tunnels with scaled-down models of buildings and wind turbines [15,16,17,18,19]. Two methods have been used in these low-speed studies to calculate the aerodynamic damping, namely by having the structure be

passively excited through free-stream fluctuations/turbulence and by actively applying an external force known as either the Force-Excitation Method or the Force-Oscillation Method. Similarly, this experimental study employed two types of structural excitation methods to measure both the effects of the aerodynamic stiffness and the aerodynamic damping on the single degree-of-freedom (SDOF) wind tunnel model. The following methodology section describes the wind tunnel used for all experimental cases in this study. A description of the model's design is then explained along with the different measurement techniques used in both wind-off and wind-on cases. A brief section on the theory behind the governing equation of this particular fluid-structure interaction is discussed, and the results are subsequently presented.

2   EXPERIMENTAL METHODS AND TECHNIQUES

The experiments were carried out at The University of Texas at Austin Mach 5 Blowdown Wind Tunnel located at the JJ Pickle Research Campus. The flow is heated to reduce the effects of oxygen condensation in the free-stream. The typical runtime is about $40 - 80$ seconds. The flow consists of heated air with stagnation conditions of $T_0 = 345 \pm 5$ K and $p_0 = 2500 \pm 25$ kPa. The boundary layer height on the walls of the test section is approximately $\delta_{99} = 19$ mm and the measured static pressure in the test section was $p_\infty = 4.5$ kPa [20]. The facility has a unit Reynolds number of $Re_\infty = 50 \times 10^6 \mathrm{m}^{-1}$. The Mach 5 blowdown wind tunnel has a test section that is 152 mm wide by 178 mm high by 762 mm in length with solid walls. This test section is equipped with interchangeable glass windows on all four sides, providing optical access for flow visualization during testing.

2.1   Cone-Cylinder SDOF Model

The wind tunnel model is designed using a solid conical section attached to a solid cylindrical section using a flexure joint as shown in Figure 1a. Both the conical and cylindrical sections were machined from 6061 aluminum. The flexible joint was made of Delrin. As shown on Figure 1a, the flexure was intentionally designed to only allow for bending in one vibrational DOF and consequently reduce the vibrational degree of freedom of the conical section to include only angular pitching motion. As shown on Figure 1b, the flexure is modeled as a torsional spring attaching a cone to a rigid wall. A Vibronics VJP16-70E310 eccentric spinning mass motor was embedded downstream of the joint in order to induce harmonic forcing on the upstream structure, as shown on Figure 1c. All experimental cases were done with the model at an angle of attack of 0 degrees.
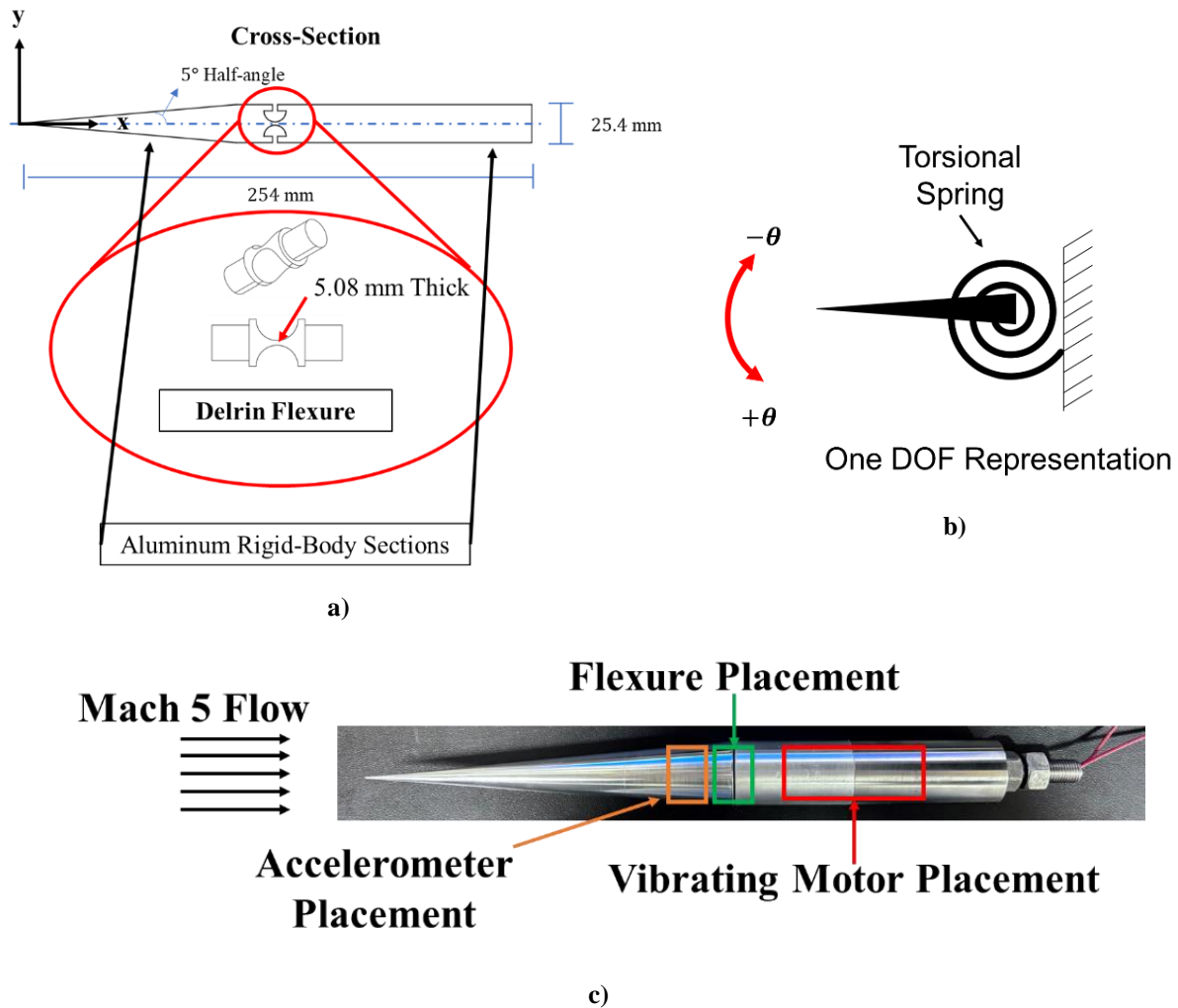
Figure 1: HARV-W compliant model, a) model dimensions and internal structure, b) SDOF simplification c) wind tunnel machined model with locations of electric motor and flexure shown

2.2 Measurement of Structural Response

The structural response was measured using three different measurement techniques depending on the wind-on or wind-off case. These techniques included edge-tracking, to determine the structural angular motion, a Laser Doppler Vibrometer (LDV) to measure the structural velocity, and an accelerometer mounted on the cone to measure the frequency response function (FRF) of the SDOF structure excited at different frequencies.

2.2.1 Edge Tracking

Tracking the angular pitching motion of the model was obtained by imaging a fast-response pressure-sensitive paint (PSP) coated on the surface of the SDOF model. PSP is being developed for future tests to measure the unsteady surface pressure, but we found the setup provided excellent contrast that improved the edge tracking accuracy. A schematic of the PSP imaging setup around the test section is shown in Figure 2. Two Photron Fastcam SA-Z cameras with a 50 mm lens and two high-intensity air-cooled LED 460 nm illumination were arranged on the top and side of the wind tunnel test section. The CMOS cameras were fixed perpendicular to the optical windows of

the test section aligned with the pitch and yaw axes of the model. The side camera was the main camera used to track the angular pitching motion of the SDOF structure. The top camera only tracked the yaw motion of the model initially, and it was later removed from experiments due to the yaw motion being negligible compared to the pitching motion. LED illumination was the sole light source of the wind-tunnel facility and was positioned such that the model was optimally illuminated.
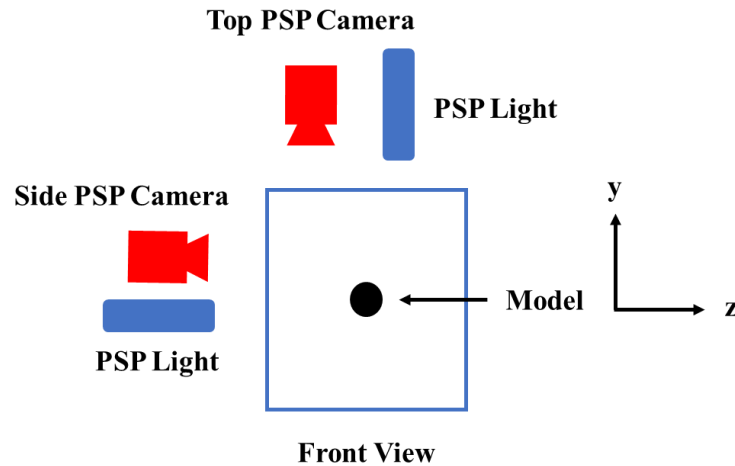

Figure 2: PSP experimental technique setup

This PSP utilizes the oxygen-quenching nature of the luminophore to fluoresce at different intensities depending on the partial pressure of oxygen and hence, the surface pressure of the gas to which the paint is exposed [23]. The fast-response ruthenium-based paint was made and applied in-house. Silicone, titanium dioxide (TiO2), and a mixture of dichloromethane and toluene were chosen to act as binder, source of porosity, and solvent, respectively. Detailed paint characteristics are provided by Egami et al. [23,24]. The luminophore (Tris(4,7-diphenyl-1,10-phenanthroline) ruthenium (II) dichloride) absorbs light at a wavelength of around 460 nm and emits light at 550~780 nm range. Based on this information, two custom-made ISSI 2-inch Air Cooled LEDs (LM2X-DM-460) lamps and an in-house lamp that emit light at a wavelength of around 460 nm were chosen as the light source to excite the paint. Figure 2 shows a schematic of the experimental setup where the emitted light was captured by a high-speed camera (Photron Fastcam SA-Z) equipped with an orange longpass filter (MidOpt LP530) that separated the signal from the blue light source. Measurements were conducted for a maximum duration of 45 seconds in some cases. Because the priority was to obtain the filtered fluoresced images for motion tracking, all the painted surface pixel values were close to saturation in order to clearly define the edges of the SDOF structure. It is important to note that high resolution was achieved with this measurement technique because only the pitching angle of the SDOF structure's rigid-body motion was tracked. The edges were detected and tracked by using an in-house MATLAB program that looks for the highest and lowest pixel intensity value gradient in each column within a specified window. The location of the highest and lowest gradients in each column marked the location of the upper and lower edges respectively in each image. Best-fit slopes of these locations measured the structure's pitching angle. With the structure's natural frequency being less than 100 Hz, images were acquired at 1000 frames per second (fps) or 5000 fps depending on the structural excitation case. Figure 3 shows a time sequence of the structural motion using the LED-enhanced images right after the starting shock has passed by. The first image at 10.099 seconds shows the moving shock impinging on the

model as seen by the stark difference in surface intensities. Subsequent images show the free-decay response of the model with the starting shock downstream and outside of the camera's view. In the end, these images show the violent forcing that the structure endures during each wind tunnel startup and the consequent large structural response it exhibits. These images also helped refine the design of the model in order for future design iterations to withstand startup loads more effectively.
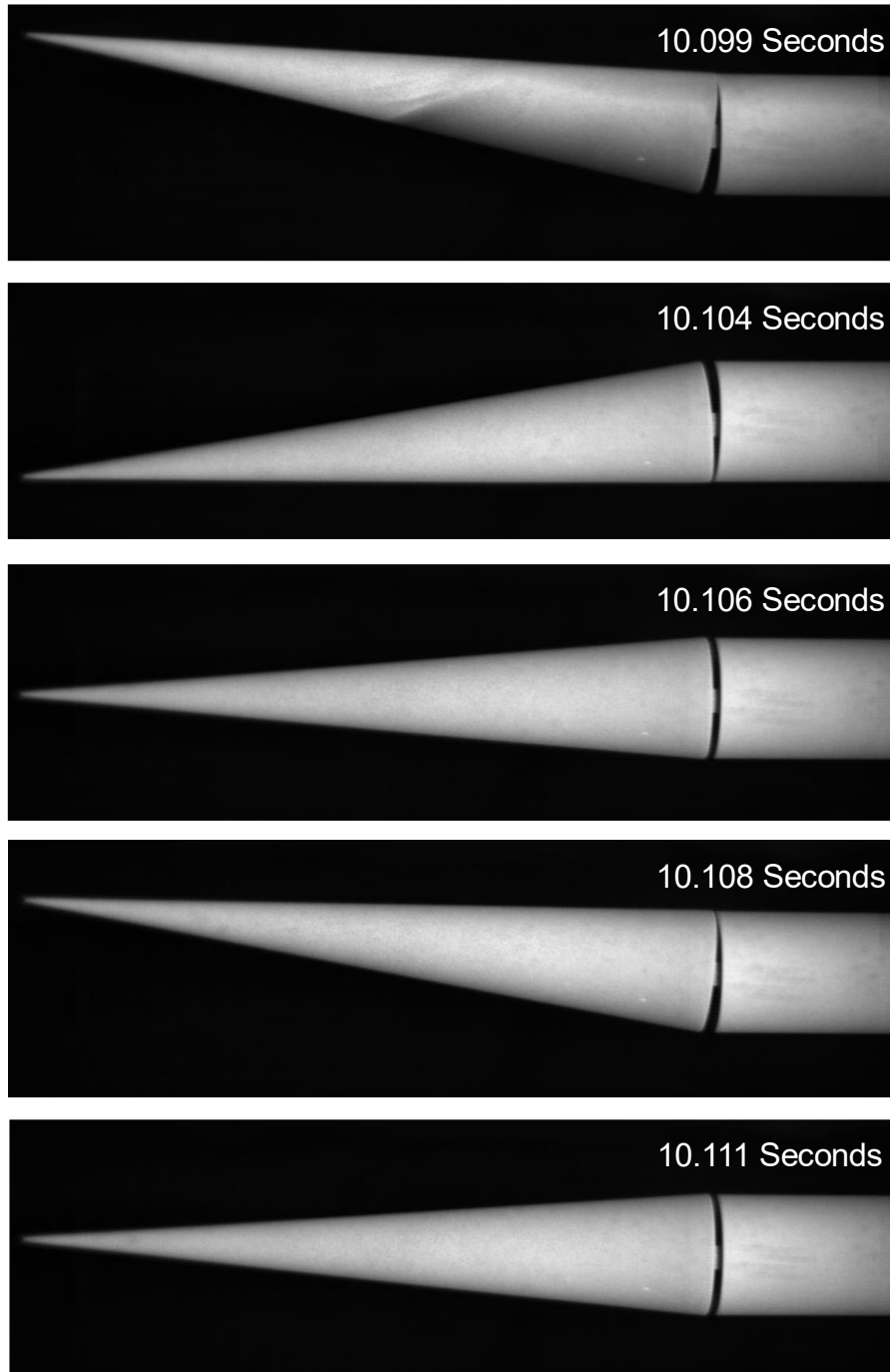

Figure 3: Time sequence of structural motion soon after starting shock passes by

2.2.2   Laser Doppler Vibrometer (LDV)

A VibroFlex Laser Doppler Vibrometer (VFX-F-110) was used to validate the edge-tracking imaging technique and wind-off accelerometer measurements. Figure 4 shows the LDV experimental setup used. The LDV laser head was placed directly above the model and outside the test section. The HeNe laser beam was focused on the top surface of the conical forebody on a centerline location that was 0.113 meters downstream of model's nose.
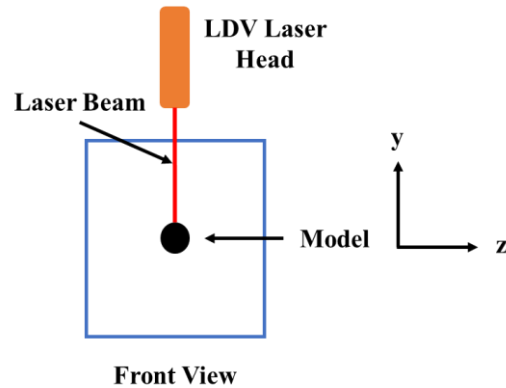
Figure 4: LDV experimental technique setup

2.2.3   Accelerometer

To characterize the wind-off frequency response function (FRF) of the SDOF structure, a piezoelectric accelerometer (PCB Piezotronics shear accelerometer, 2-gram mass, range 0.5-10000Hz) was placed 0.12 meters from the model's nose on the upper surface of the conical forebody, as shown on Figure 1c. Measurements were performed with the accelerometer placed close to the joint/flexure so as to minimally affect the structure's rotational inertia. Accelerometer data was recorded at 5 kHz.

2.3   Structural Excitations

Two different methods of exciting the SDOF structure were implemented during the wind-tunnel runs. The first method used the forcing from free-stream turbulent Mach 5 flow to excite the structure. The second method used the harmonic forcing from the embedded vibrating motor to excite the structure and later generate a free-decay response by instantaneously stopping the forcing. Using both methods allowed for changes in the structural natural frequency and damping ratio compared to wind-off values to be measured. Consequently, these two methods allowed the effects of aerodynamic stiffness and aerodynamic damping on the structural response be quantified.

2.3.1   Structural Excitation from Free-Stream Turbulent Flow

The first structural excitation method was carried out by having the structurally-compliant model exposed to free-stream turbulent Mach 5 flow. The free-stream flow of this wind tunnel has been shown to have turbulence and what are known as entropy spots [20]. These are random in time and space. The change in natural frequency and damping ratio from wind-off values were calculated by reconstructing a free-decay response from the measured structural response. Two different algorithms were used for this reconstruction, the Random Decrement Technique and the Natural Excitation Technique. Both require turbulence to be the only source of excitation [14,25,26].

2.3.2 *Structural Excitation from Harmonic Forcing*

The second structural excitation method involved embedding an electric motor that spins an eccentric mass and induces harmonic forcing on the model. The motor was spun at a range of frequencies ± 20 Hz from the structure's natural frequency, and the Frequency Response Function (FRF) plot was created by tracking the structural response amplitude at each different excitation frequency [27]. In addition, free-decay oscillations of the structure were recorded after abruptly stopping the harmonic forcing. The damping ratio was extracted from the resulting free vibration using three algorithms: the Moving-Block technique, the Hilbert Transform, and the Continuous Wavelet Transform.

3 THEORY

The following is the equation of motion (EOM) that describes the physics of the problem using standard notations [33,35]:

$$\ddot{\theta}(t) + 2\zeta_0\omega_n\dot{\theta}(t) + \omega_n^2\theta(t) = P(t)/I_0 \qquad (1)$$

Where I_0 is the rotational inertia of the conical forebody, $\theta(t)$ is the structure's angular pitching displacement, ζ_0 is the structural damping (fraction of critical), and ω_n is the angular frequency $2\pi f$. The generalized force P(t) is given by the virtual work done by the aerodynamic forces and moments, where W is the work done and $P = \frac{\partial W}{\partial \theta}$. It has been derived that for an SDOF undergoing torsional pitching motion, the EOM can include aerodynamic damping ratios that linearly add to the structural damping ratio as shown below:

$$\ddot{\theta}(t) + 2(\zeta_0 + \zeta_a)\omega_n\dot{\theta}(t) + \omega_n^2\theta(t) = P_f(t)/I_0 \qquad (2)$$

Where ζ_a is the aerodynamic damping ratio generated by both attached and separated flow on the model's surface and $P_f(t)$ is the generalized aerodynamic forcing moment independent of body motion. Wind-off values that were measured from the recorded angular displacements $\theta(t)$ were the natural frequency $\omega_{n_{off}}$ and damping ratio ζ_0. Wind-on values that were measured from the recorded angular displacements $\theta(t)$ were the new natural frequency $\omega_{n_{on}}$ and the new damping ratio $\zeta_{on} = \zeta_0 + \zeta_a$. Because all measured pitching amplitudes $\theta(t)$ of the SDOF model were small O(<1 degree), the FSI system was considered to be within the linear range, and the EOM framework shown holds.

4 RESULTS

4.1 Wind-off Structural Characterizations

Wind-off structural characterization was conducted by measuring the free-vibration response of the SDOF model after abruptly stopping the harmonic forcing from the embedded electric motor. Measurement of the wind-off structural response involved measuring the structural velocity with the LDV and measuring the structural acceleration with the accelerometer. Figure 5 shows the normalized free-decay response measured at the same time by both the LDV and the accelerometer. The response was measured four oscillatory cycles after the harmonic forcing was instantaneously stopped. To synchronize both readings, the LDV measurements were phase-shifted 90° to match the accelerometer measurements. All wind-off measurements were analyzed to calculate the natural frequency and structural damping of the SDOF model. Three different algorithms were used to calculate the structural damping ratio, namely the Moving-Block

technique, the CWT – Morlet Wavelet technique, and the Hilbert Transform. To determine a noise floor, a set of 1000 data measurements from both the LDV and the accelerometer were recorded of the motionless structure. The temporal standard deviation of the noise floor for the voltage signal was approximately 0.00026 Volts for the LDV and 0.00031 Volts for the accelerometer. The peak SNR was computed to be 23 dB for the LDV measurement and 31 dB for the accelerometer measurement.
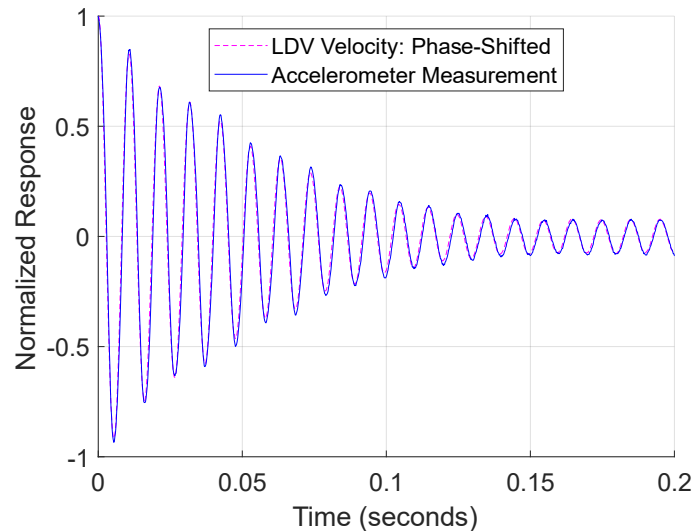

Figure 5: Wind-off normalized free-decay response from instantaneously stopping the harmonic forcing

4.1.1 Moving-Block Technique Results

The Moving-Block technique is a method which allows the determination of modal dampings and frequencies from a response signal of a structure that is undergoing a transient response. The transient excitation may consist of a sinusoidal input which has been abruptly terminated or it may be an impulsive excitation. In any event, if the damping and frequency of a particular mode are desired, it is necessary that this mode be excited by the type of excitation chosen. Therefore, the advantages of using the Moving-Block method are that damping and frequency of multiple modes can be measured [29]. However, this requirement that the structure be excited and then be allowed to decay freely is one of the disadvantages of the method. In this case, the structural frequency was obtained by conducting a Fast-Fourier Transform (FFT) of the signal and measuring the frequency placement of the peak as shown on Figure 6a. The Δf or frequency bin of the FFT was 5 Hz. The damping calculation was made by using the optimized frequency and block and by computing successive discrete Fourier transforms as the block is moved down the data record. The block was first positioned at the beginning of the record, the transform was computed, and the logarithm of the transform amplitude was plotted as shown on Figure 6b. The block was then moved down the data record one data sample and this process was repeated. The damping in the mode being analyzed was obtained from the slope of a linear least-squares to this curve, where the magnitude of the slope is equal to the frequency multiplied by the damping ratio. Table 1 shows the measured natural frequencies and damping ratios for each measurement and damping extraction algorithm.
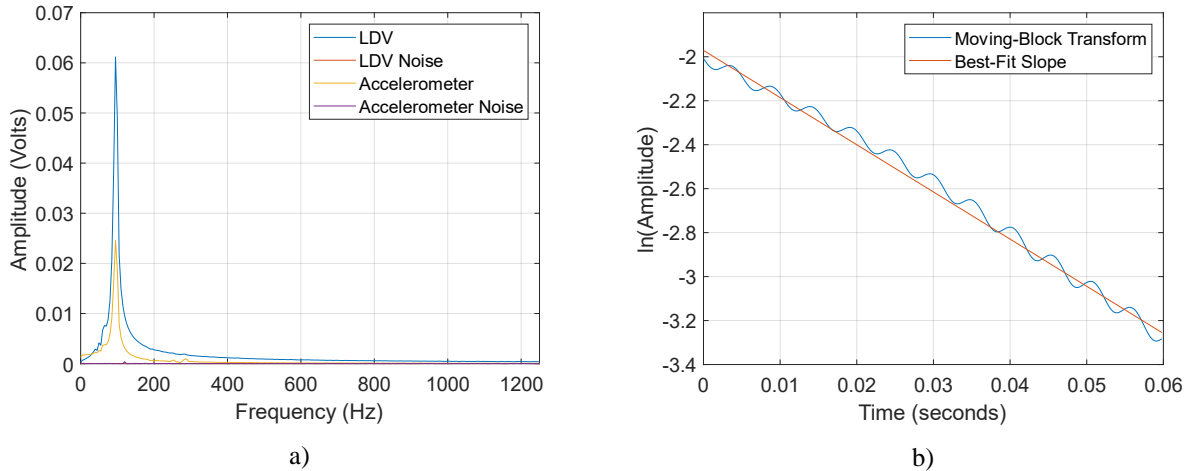
9

Figure 6: Moving-Block Technique Results, a) FFT plot of the wind-off free-decay response b) Moving-Block transform of the free-decay response and the calculated best-fit slope from which the damping ratio was calculated

4.1.2   *Continuous Wavelet Transform (CWT) – Morlet Wavelet Results*

The Continuous Wavelet Transform (CWT) for damping identification uses pattern-search updating for the correction of the identification results and the frequency-slice wavelet transform for the transient vibration response analysis [30]. The CWT methods have proven to be resistant to noise and can identify damping at closely spaced natural frequencies for different modes [31]. The CWT methods require the following steps: the calculation of the CWT transform at a time–frequency grid, followed by the ridge and skeleton detection phase, and, finally, after the edge effected region has been removed from the identification area, the damping ratio can be identified from the logarithmic decay [32]. CWT has been shown to be one of the best methods for analyzing the damping of multi-degree-of-freedom systems. However, it is susceptible to the edge effect, which causes a non-valid identification at the start and the end of the time-series. There are different CWT techniques depending on the wavelet used. For this study, the Morlet-wavelet was chosen. Figure 7a shows the time-frequency grid from the CWT technique. The red-colored area identifies the beginning of the map's ridge which coincides with the SDOF's natural frequency. If the structure was to have more than one mode, multiple hot-spots and ridges would have been shown on the time-frequency grid. Therefore, the CWT transform validates the SDOF nature of the model. Figure 7b shows the logarithmic decay of the ridge and the best-fit slope whose magnitude is equal to the natural frequency multiplied by the damping ratio. Table 1 shows the measured natural frequencies and damping ratios for each measurement technique using the CWT method. Again, each damping measurement is consistent between different measurements and agree well with processed data from the Moving-Block technique.
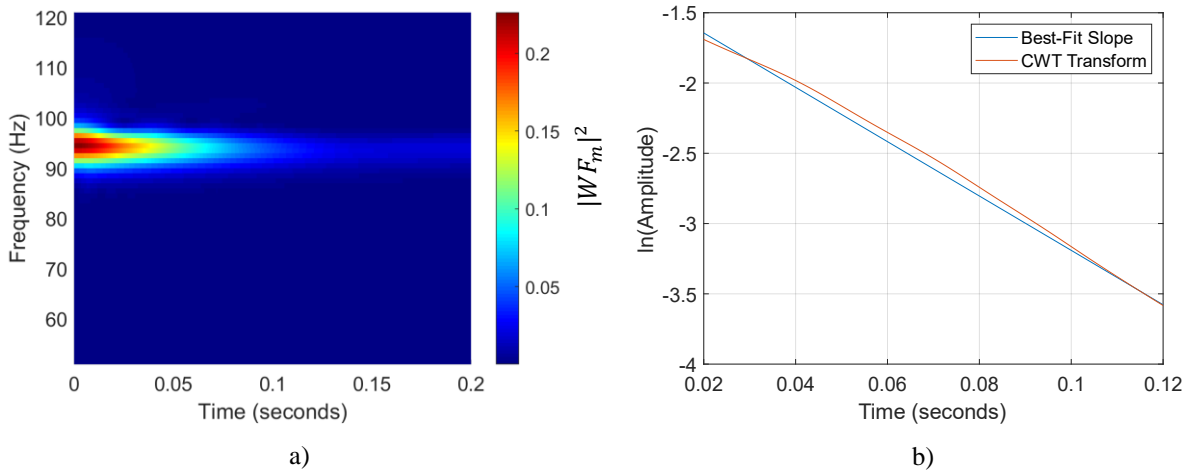
Figure 7: CWT – Morlet Wavelet, a) CWT time-frequency grid of LDV-measured free-decay response b) CWT transform of the free-decay response and the calculated best-fit slope from which the damping ratio was calculated

4.1.3 Hilbert Transform Results

The damping ratio from the Hilbert Transform is calculated by taking the logarithmic decay of the Hilbert envelope, with the magnitude of the slope of the logarithmic decay equal to the natural frequency multiplied by the damping ratio [34]. Figure 8a shows the Hilbert envelope along with the free-vibration response. The Hilbert envelope is then plotted on a logarithmic graph as shown on Figure 8b and the best-fit slope is calculated. It is important to note that although damping and natural frequency values obtained from the Hilbert Transform show consistency between different measurements as shown on Table 1, the damping values are slightly lower than the ones measured with the Moving-Block and CWT techniques.
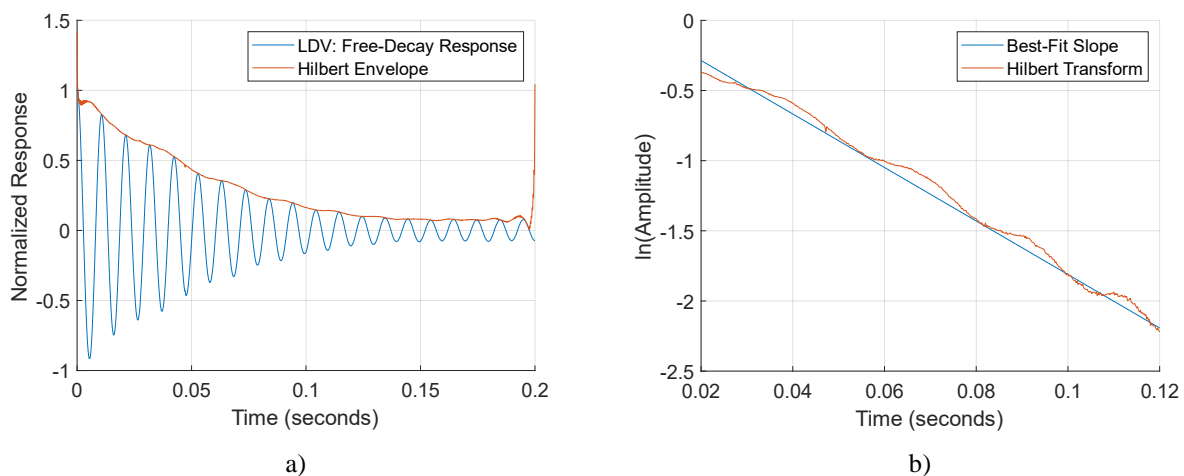

Figure 8: Hilbert Transform, a) Hilbert envelope plot of free-decay response b) Hilbert transform of the free-decay response and the calculated best-fit slope from which the damping ratio was calculated

Table 1: Wind-off Structural Characterization

		Natural Frequency (Hz)	Damping Ratio (%)
Moving-Block	LDV	94.9 ±2.5	3.60
	Accelerometer	94.9 ±2.5	3.55
CWT – Morlet Wavelet	LDV	94.9 ±2.5	3.24
	Accelerometer	94.9 ±2.5	3.18
Hilbert Transform	LDV	94.9 ±2.5	3.20
	Accelerometer	94.9 ±2.5	3.12

4.2   Free-Stream Turbulence Forcing Results and Analysis

The model was exposed to Mach 5 free-stream flow and its structural response measured via imaging at 5000 fps. Figure 9a shows a one-second subset of the entire 8.7 seconds in which the model was exposed to Mach 5 flow and had achieved a stationary state. Although perturbations to the pitching angle were small, the data shows evidence of unsteady forcing from free-stream turbulence. To determine a noise floor, a set of 1000 images was recorded of the motionless structure at 1000 fps. The temporal standard deviation of the noise floor for the pitching angle displacement was approximately 0.00096 degrees as shown in Figure 10b. From this data, two techniques were used to generate a free-decay response from which natural frequency and damping ratios could be extracted, namely the Random Decrement Technique (RDT) and the Natural Excitation Technique (NExT). Both require random turbulence to be the only source of excitation or some sort of Gaussian/white-noise forcing for both techniques to be applied. Figure 9b shows the generated responses using both methods. The RDT technique is carried out entirely in the time domain, thus, RDT is solely based on response measurements. The underlying principle of RDT lies in the extraction of free decay from random response by averaging a large number of samples with identical initial conditions (or "trigger conditions") [26]. The disadvantage of using RDT are that it can be difficult to analyze when more than one mode is present. The NExT method assumes that the impulse response function and the cross-correlation function in linear systems have similar expressions. Therefore, by assuming that the external excitation is a white noise, the impulse response function is replaced by the cross-correlation function [25]. Figure 10a shows the FFT of the RDT and NExT impulse response functions. Both demonstrate that even the generated structural responses match the natural frequency of the original signal. It is important to point out that the measured natural frequency from both techniques was lower than the measured wind-off natural frequency, with the Δf of the FFT being 1 Hz. The damping ratios were calculated by using the Moving Block method, the CWT method, and the Hilbert transform. All analyses show an increase in the damping ratio compared to wind-off values as shown on Table 2, which is indicative of a positive aerodynamic damping ratio that increases the structure's overall damping.
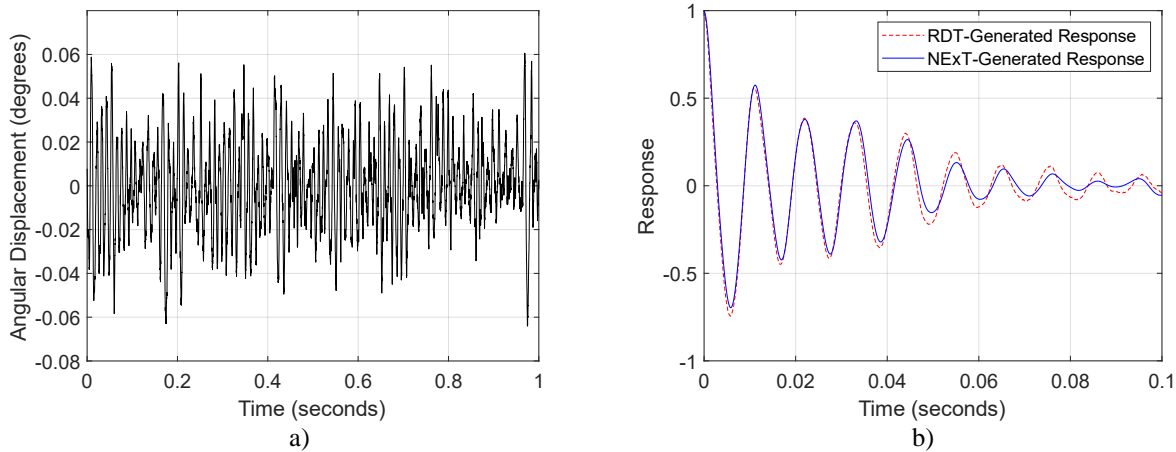
Figure 9: Free-stream Mach 5 turbulent flow forcing, a) Imaging measurement of structural response b) RDT and NExT transform of the free-stream structural response
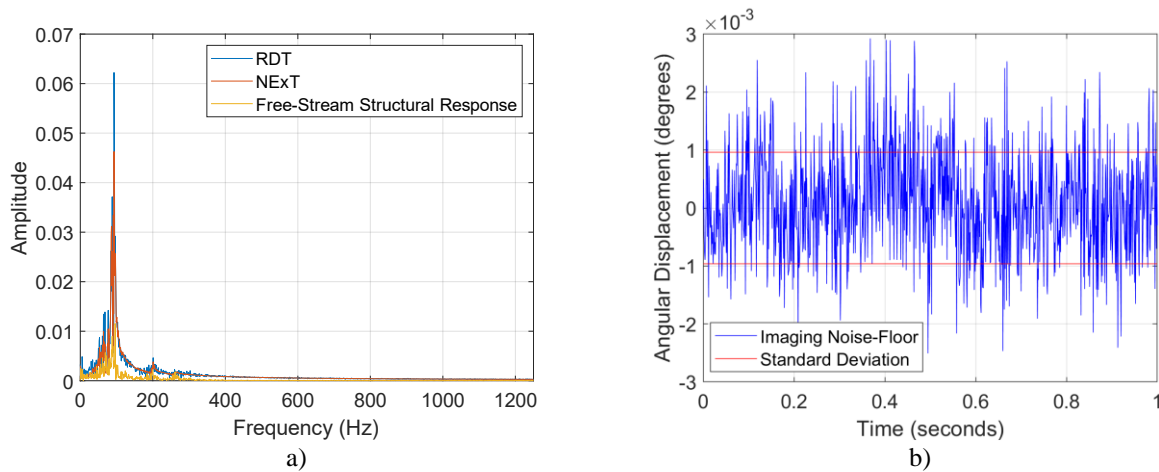

Figure 10: Free-stream Mach 5 turbulent flow forcing, a) FFT plot of RDT, NExT, and structural response b) Noise-floor of imaging measurements

4.3   Harmonic Forcing Wind-on Results and Analysis

Harmonic forcing on the SDOF model was achieved by embedding a vibrating motor that spins an eccentric mass and induces harmonic forcing on the model. For both the wind-off case and the wind-on case, the motor was spun at a range of frequencies ±20 Hz from the structure's natural frequency. The corresponding structural response for each frequency was tracked by an accelerometer in the wind-off case and by imaging in the wind-on case. From these results, the Frequency Response Function (FRF) plot was created as shown on Figure 11a and 11b [27]. The wind-on FRF plot was obtained by sequentially changing the harmonic forcing frequency during the entire 45 seconds of the wind tunnel run. Sufficient time between frequency changes was ensured in order for any transients to die out. The wind-on FRF plot shows more noise than its wind-off counterpart. However, the peak frequency is shown to hover at around 91 Hz. Like the turbulent forcing case, this shift to a lower peak frequency from wind-off to wind-on data is evidence of a negative aerodynamic stiffness term that reduces the structure's natural frequency.
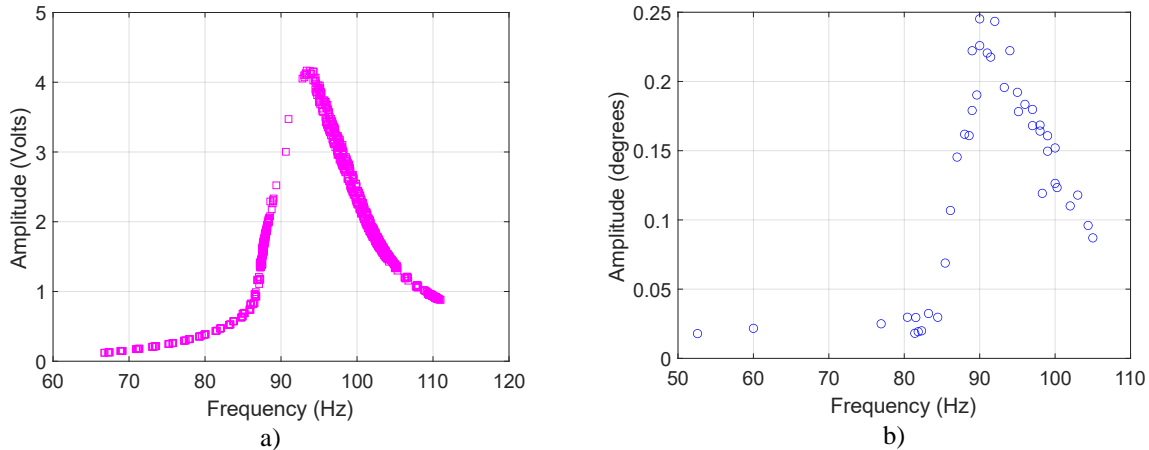
Figure 11: Reconstructed FRF Plots, a) Wind-off FRF plot with harmonic forcing b) Wind-on FRF plot with harmonic forcing

Figure 12a compares the structural response exposed to the same harmonic forcing in both wind-off and wind-on cases. It is seen that the wind-on structural response sporadically varies more in amplitude than its wind-off counterpart for the same harmonic forcing frequency. This is evidence of turbulent perturbations on the structural response which are also evident in the wind-on FRF plot shown on Figure 11b. It is important to note that the structural response shown on figure 12a is about 10 times larger than the structural response seen on Figure 9a because the harmonic excitation from the electric motor induces forces that are greater than the free-stream turbulent perturbations. Similarly, the free-stream turbulence effects are also seen in Figure 12b, where the wind-on free-decay response of the structure is tracked after the harmonic forcing is instantaneously stopped. This free-decay is not a clean free-decay as seen in the wind-off cases due to free-stream turbulence. Because of this only the Moving-Block and CWT techniques were used to calculate the damping ratio as shown on Table 2. Applying the Hilbert transform resulted in no best-fit line to measure on a logarithmic plot. Nevertheless, the other two damping-extraction algorithms showed a decrease in natural frequency and an increase in damping ratio compared to wind-off values. Like the wind-on results from the free-stream forcing cases, this decrease in natural frequency further indicates the effects of aerodynamic stiffness on this model. Likewise, the increase in damping ratio illustrates the stabilizing effects of aerodynamic damping on the model.
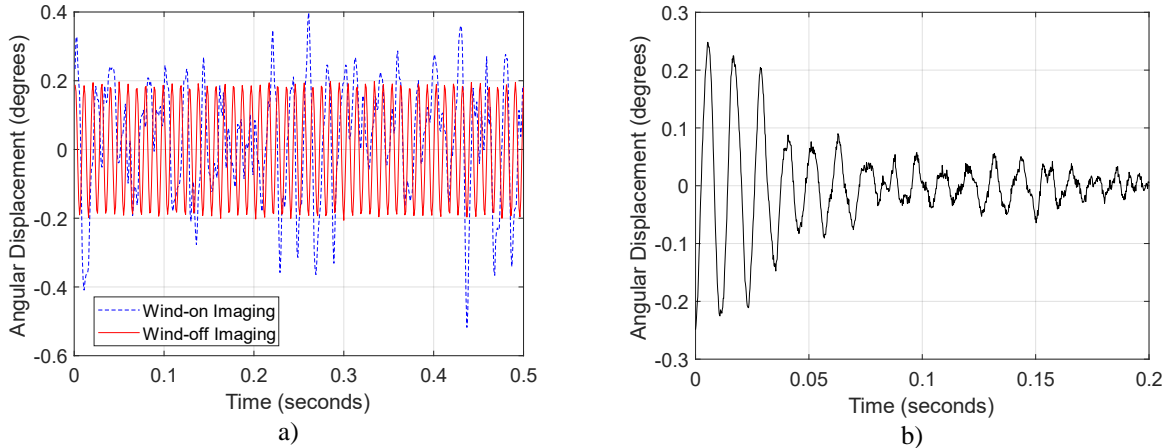
Figure 12: Harmonic forcing method, a) Comparison of structural response with same harmonic forcing frequency between wind-off and wind-on cases b) Free-decay response of structure after the harmonic forcing is instantaneously stopped

Table 2: Wind-on Structural Characterization

			Natural Frequency (Hz)	Damping Ratio (%)
Free-Stream Flow Forcing	Moving-Block	RDT	91.9 ±0.5	5.55
		NExT	91.9 ±0.5	6.42
	CWT – Morlet Wavelet	RDT	91.9 ±0.5	4.82
		NExT	91.9 ±0.5	4.67
	Hilbert Transform	RDT	91.9 ±0.5	4.35
		NExT	91.9 ±0.5	5.38
Harmonic Forcing	Moving-Block	Free-Decay	88.9 ±0.5	4.90
	CWT – Morlet Wavelet	Free-Decay	88.9 ±0.5	5.04

5   CONCLUSIONS

Overall, the damping ratio of all wind-on cases of a SDOF structurally-compliant model in Mach 5 flow were found to be higher than the wind-off cases. In a similar manner, the SDOF model's wind-on natural frequencies were measured to be lower than the wind-off natural frequencies. These results indicate the existence of an aerodynamic stiffness moment that reduces the overall effective stiffness of the structure, while at the same time indicating the existence of an aerodynamic damping moment that increases the structure's overall damping. This increase in damping compared to wind-off values occurred for both wind-on structural response amplitudes that were 10 times less than the wind-off amplitudes and for wind-on structural responses whose amplitudes were slightly larger than the wind-off amplitudes. This indicates that the aerodynamic damping ratio appears to be independent of amplitude. Both RDT and NExT methods for

15

processing the free-stream forcing response produced similar results, and therefore validated each other for applications in future hypersonic wind tunnel experiments. Using the Moving-Block technique and CWT for the wind-on harmonic forcing cases proved to be reliable for structural responses that are perturbed by free-stream turbulence encountered in high-speed wind tunnels. Because of these perturbations in the flow, reconstructing the wind-on FRF plot over a single long-duration wind tunnel run proved to be challenging. Therefore, future enhancements will include increasing the harmonic forcing amplitude to be several times greater than the turbulent perturbation forcing amplitudes. It is important to note that these structural excitations can only be employed in hypersonic wind tunnels that have duration times that are significantly longer compared to the structural time scale. Consequently, our Mach 5 blowdown wind tunnel with run times of over one minute was shown to be the right facility to carry out these experiments.

Future work includes an investigation into the effects of varying the angle-of-attack on the model's wind-on structural characteristics. Similarly, it will be useful to compare measured aerodynamic stiffness moments and aerodynamic damping moments to theoretical values that use low-order aerodynamic models of hypersonic cone stability derivatives. By doing so, determining the aerodynamic stability models that agree best with experimental data allows for the development of better scaling conversions of wind tunnel aeroelastic data to free-flight experiments. In addition, knowing the surface-integrated and unsteady aerodynamic force on the model would allow the forcing function to be measured. Therefore, future studies into unsteady surface pressure imaging with time-resolved force balance measurements of a dynamically deforming model should be carried out. And finally, exploring the limitations of both free-stream forcing method and harmonic forcing method within more complicated hypersonic flows such as shock-impingements and cavity-store separation would help plan for future aeroelastic studies in hypersonic wind tunnels. Similarly, applying forcing methods to more complicated structures with higher DOF in a methodical manner will help analyze continuously flexible wind tunnel models that are more representative of real-life hypersonic aircraft structures. In conclusion, these breadth of experiments of the FSI of axisymmetric bodies all fit into an integrated framework that helps characterize the limits of scaled-down hypersonic aeroelastic testing in long-duration blowdown hypersonic wind tunnels.

6   ACKNOWLEDGEMENTS

REFERENCES

[1]   Bowcutt, Kevin. "A perspective on the future of aerospace vehicle design." AIAA paper 2003-6957, *12th AIAA International Space Planes and Hypersonic Systems and Technologies*, December 2003.

[2]   Bisplinghoff, Raymond L., Holt Ashley, and Robert L. Halfman. *Aeroelasticity*. Courier Corporation, 2013.

[3]   Bisplinghoff, R. L. "Some structural and aeroelastic considerations of high-speed flight the nineteenth wright brothers lecture." *Journal of the Aeronautical Sciences* 23, no. 4 (1956): 289-321.

[4]   Mikhail, Ameer G. "In-flight flexure and spin lock-in for antitank kinetic energy projectiles." *Journal of spacecraft and rockets* 33, no. 5 (1996): 657-664.

[5]   Mooij, Erwin. "Robust control of a conventional aeroelastic launch vehicle." AIAA paper 2020-1103, *AIAA Scitech Forum*, January 2020.

[6]   Melcher, John T., Eliott J. Radcliffe, Cameron Butler, and Bradley M. Wheaton. "Effects of Aeroelasticity on Flight Dynamics in the Boundary Layer Transition (BOLT) Experiment." AIAA paper 2022-3748, *AIAA AVIATION 2022 Forum*, June 2022.

[7]   Casper, Katya M., Steven J. Beresh, John F. Henfling, Russell W. Spillers, Patrick Hunter, and Seth Spitzer. "Hypersonic fluid–structure interactions due to intermittent turbulent spots on a slender cone." *AIAA Journal* 57, no. 2 (2019): 749-759.

[8]   Chism, James R., Phillip A. Kreth, and John D. Schmisseur. "Characterization of Downstream Effects from a WavyWall on a Hollow Cylinder at Mach 4." AIAA paper 2023-0080, *AIAA SCITECH 2023 Forum*, January 2023.

[9]   Tihomirov, Dimitry, and Daniella E. Raveh. "Nonlinear aerodynamic effects on static aeroelasticity of flexible missiles." AIAA paper 2019-0486, *AIAA SciTech 2019 Forum*, January 2019.

[10] Heddadj, S., R. Cayzac, and J. Renard. "Aeroelasticity of high L/D supersonic bodies-Theoretical and numerical approach." In *38th Aerospace Sciences Meeting and Exhibit*, p. 390. 2000.

[11] McNamara, Jack J., Andrew R. Crowell, Peretz P. Friedmann, Bryan Glaz, and Abhijit Gogulapati. "Approximate modeling of unsteady aerodynamics for hypersonic aeroelasticity." *Journal of Aircraft* 47, no. 6 (2010): 1932-1945.

[12] Shelton, Andrew, Christopher Martin, and Walter Silva. Characterizing aerodynamic damping of a supersonic missile with CFD. No. NF1676L-28268. 2018.

[13] Lightfoot, James R., and Charles E. White. "Special Applications of Strain-gage Balances Used in the Supersonic and Hypersonic Wind Tunnels at the US Naval Ordnance Laboratory." AGARD, 1956.

[14] Hammond, Charles E., and Robert V. Doggett Jr. "Determination of subcritical damping by moving-block/randomdec applications." Its Flutter Testing Tech., (1976).

[15] Rasmussen, Flemming, J. Thirstrup Petersen, and H. Aagaard Madsen. "Dynamic stall and aerodynamic damping." (1999): 150-155.

[16] Tamura, Yukio, and Shin-ya Suganuma. "Evaluation of amplitude-dependent damping and natural frequency of buildings during strong winds." *Journal of wind engineering and industrial aerodynamics* 59, no. 2-3 (1996): 115-130.

[17] Marukawa, H., N. Kato, K. Fujii, and Y. Tamura. "Experimental evaluation of aerodynamic damping of tall buildings." *Journal of wind engineering and industrial aerodynamics* 59, no. 2-3 (1996): 177-190.

[18] Staubli, T. "Calculation of the vibration of an elastically mounted cylinder using experimental data from forced oscillation." (1983): 225-229.

[19] Fontecha, Robert, Frank Kemper, and Markus Feldmann. "On the determination of the aerodynamic damping of wind turbines using the forced oscillations method in wind tunnel experiments." *Energies* 12, no. 12 (2019): 2452.

[20] Diaz Villa, Benjamin E., Marc A. Eitner, Jayant Sirohi, and Noel Clemens. "Shock Impingement Interaction on a One Degree-of-Freedom Slender Hypersonic Vehicle in Mach 5 Flow." AIAA Paper 2024-2848, *AIAA SCITECH 2024 Forum*, January 2024.

[21] Vasile, Joseph D., Frank Fresconi, James DeSpirito, Marco Duca, Thomas Recchia, Brian Grantham, Rodney DW Bowersox, and Edward B. White. *High-Speed Army Reference Vehicle*. US Army Combat Capabilities Development Command, Army Research Laboratory, 2022.

[22] Anderson, John David. *Hypersonic and high temperature gas dynamics*. AIAA, 1989.

[23] Egami, Y., Sato, Y., and Konishi, S., "Development of Sprayable Pressure-Sensitive Paint with a Response Time of Less Than 10 μs," AIAA Journal, Vol. 57, No. 5, 2019, pp. 2198–2203

[24] Egami, Y., Hasegawa, A., Matsuda, Y., Ikami, T., and Nagai, H., "Ruthenium-based fast-responding pressure-sensitive paint for measuring small pressure fluctuation in low-speed flow field," Meas. Sci. Technol., Vol. 32, No. 2, 2020, p. 024003.

[25] James, George H. "The natural excitation technique (NExT) for modal parameter extraction from operating structures." *J Anal Exp Modal Anal* 10, no. 4 (1995): 260.

[26] Dande, Himanshu Amol. "Panel Damping Loss Factor Estimation Using the Random Decrement Technique." PhD diss., University of Kansas, 2010.

[27] Meirovitch, Leonard. "Fundamentals of vibrations/Meirovitch, L." (2000).

[28] Ericsson, L. E., and D. Pavish. "Aeroelastic vehicle dynamics of a proposed delta II 7920-10L launch vehicle." *Journal of Spacecraft and Rockets* 37, no. 1 (2000): 28-38.

[29] Bousman, W., and D. Winkler. "Application on the moving-block analysis." In *Dynamics Specialists Conference*, p. 653. 1981.

[30] Le, Thien-Phu, and Pierre Argoul. "Continuous wavelet transform for modal identification using free decay response." Journal of sound and vibration 277.1-2 (2004): 73-100.

[31] Boltežar, Miha, and Janko Slavič. "Enhancements to the continuous wavelet transform for damping identifications on short signals." Mechanical Systems and Signal Processing 18.5 (2004): 1065-1076.

[32] Slavič, Janko, Igor Simonovski, and Miha Boltežar. "Damping identification using a continuous wavelet transform: application to real data." Journal of Sound and Vibration 262.2 (2003): 291-307.

[33] Ericsson, L. E., and J. P. Reding. "Aeroelastic stability of space shuttle protuberances." *Journal of Spacecraft and Rockets* 19.4 (1982): 307-313.

[34] Bowles, Patrick O., Thomas C. Corke, Dustin G. Coleman, Flint O. Thomas, and Mark Wasikowski. "Improved understanding of aerodynamic damping through the Hilbert transform." *AIAAiaa Journal* 52, no. 11 (2014): 2384-2394.'

[35] O Edwards, John W., et al. "Aeroelastic Response and Protection of Space Shuttle External Tank Cable Trays." *Journal of Spacecraft and Rockets* 45.5 (2008): 988-998.

COPYRIGHT STATEMENT